

Multifunctional Unmanned Aerial Vehicle Wing Spar for Low-Power Generation and Storage

Steven R. Anton*

Los Alamos National Laboratory, Los Alamos, New Mexico 87545

Alper Erturk†

Georgia Institute of Technology, Atlanta, Georgia 30332

and

Daniel J. Inman‡

University of Michigan, Ann Arbor, Michigan 48109

DOI: 10.2514/1.C031542

This paper presents the investigation of a multifunctional energy harvesting and energy-storage wing spar for unmanned aerial vehicles. Multifunctional material systems combine several functionalities into a single device in order to increase performance while limiting mass and volume. Multifunctional energy harvesting can be used to provide power to remote low-power sensors on unmanned aerial vehicles, where the added weight or volume of conventional harvesting designs can hinder flight performance. In this paper, a prototype self-charging wing spar containing embedded piezoelectric and battery elements is modeled, fabricated, and tested to evaluate its energy harvesting and storage performance. A coupled electromechanical model based on the assumed modes method is developed to predict the vibration response and voltage response of a cantilevered wing spar excited under harmonic base excitation. Experiments are performed on a representative self-charging wing spar, and the results are used to verify the electromechanical model. The power-generation performance of the self-charging wing spar is investigated in detail for harmonic excitation in clamped–free boundary conditions. Experiments are also conducted to demonstrate the ability of the wing spar to simultaneously harvest and store electrical energy in a multifunctional manner. It is shown that, for an input base acceleration level of $\pm 0.25 g$ at 28.4 Hz at the base of the structure, 1.5 mW of regulated dc power is delivered from the piezoelectric layers to the thin-film battery, resulting in a stored capacity of 0.362 mAh in 1 h.

Nomenclature

A	=	area
a_b	=	base acceleration
b	=	width
\mathbf{C}	=	damping matrix
C_p	=	capacitance
c_{11}^E	=	elastic modulus at constant electric field
D	=	electric displacement
d_{31}	=	piezoelectric strain constant
E	=	electric field
e_{31}	=	piezoelectric stress constant
\mathbf{F}	=	forcing vector
H	=	Heaviside function
h	=	thickness
I	=	mass moment of inertia
J_p	=	piezoelectric coupling term
\mathbf{K}	=	stiffness matrix
L	=	length
\mathbf{M}	=	mass matrix
M	=	lumped mass
N	=	number of modes

Q	=	electric charge
R_l	=	load resistance
S_{xx}	=	strain
s_{11}^E	=	elastic compliance at constant electric field
T	=	kinetic energy
t	=	time
T_{xx}	=	stress
U	=	potential energy
v	=	voltage
V_{abs}	=	absolute beam velocity
W_{ie}	=	internal electrical energy
w_{abs}	=	absolute displacement
w_b	=	base displacement
w_{rel}	=	relative displacement
Y	=	elastic modulus
α	=	mass proportional damping constant
β	=	stiffness proportional damping constant
δW_{ncc}	=	virtual work of nonconservative electrical forces
ϵ_{33}^S	=	dielectric permittivity at constant strain
$\boldsymbol{\eta}$	=	vector of generalized coordinates
$\boldsymbol{\Theta}$	=	electromechanical coupling vector
ρ	=	mass density
Φ	=	matrix of admissible functions
ω	=	frequency

Subscripts

p	=	piezoelectric layer
s	=	structure layer

Superscripts

eq	=	equivalent representation
p	=	parallel electrode connection
s	=	series electrode connection
T	=	matrix transpose

Presented as Paper 2011-2004 at the 52nd Structures, Structural Dynamics, and Materials Conference, Denver, CO, 4–7 April 2011; received 10 June 2011; accepted for publication 27 July 2011. Copyright © 2011 by Steven R. Anton. Published by the American Institute of Aeronautics and Astronautics, Inc., with permission. Copies of this paper may be made for personal or internal use, on condition that the copier pay the \$10.00 per-copy fee to the Copyright Clearance Center, Inc., 222 Rosewood Drive, Danvers, MA 01923; include the code 0021-8669/12 and \$10.00 in correspondence with the CCC.

*Postdoctoral Research Associate, Engineering Institute, P.O. Box 1663, Mail Stop T001.

†Assistant Professor, George W. Woodruff School of Mechanical Engineering, 771 Ferst Drive, J. Erskine Love Manufacturing Building.

‡Kelly Johnson Collegiate Professor and Chair, Department of Aerospace Engineering, 1320 Beal Avenue. Fellow AIAA.

I. Introduction

WITH recent growth in the development of low-power electronic devices such as microelectronics and wireless sensor nodes, the topic of energy harvesting has received much attention in the research community. Several modes of energy harvesting exist, including conversion of solar, thermal, vibration, and wind energy to electrical energy. Among these schemes, piezoelectric vibration-based harvesting has been most heavily researched [1,2]. One particular area of interest for piezoelectric energy harvesting lies in scavenging vibration energy during flight of unmanned aerial vehicles (UAVs). Focus has recently been placed on small UAVs that can be carried and deployed by soldiers in the field and used for surveillance purposes. Vibration energy harvesting in UAVs can be used to provide local power to remote low-power sensors such as accelerometers, structural health monitoring nodes, or perhaps small imaging devices, such as cameras. Anton and Inman have previously performed a proof of concept flight experiment where a nonoptimized UAV wing spar with surface-mounted piezoelectric patches was shown to generate $11.3 \mu\text{W}$ in level flight, which is useful for low-power sensor systems [3].

Traditional piezoelectric energy harvesting systems consist of an active harvesting element, conditioning circuitry, and a storage medium, where the sole function of the combined system is to convert ambient mechanical energy into usable electrical energy. Furthermore, conventional systems are designed as add-on components to a host structure, often causing undesirable mass loading effects and consuming valuable space. A method of improving the functionality of conventional harvesting designs involves the use of a multifunctional approach in which the system not only performs energy harvesting but also performs additional tasks such as storing the scavenged energy or supporting mechanical load in the host structure.

Previous studies have been conducted by Thomas and Qidwai [4,5], Qidwai et al. [6], and Rohatgi et al. [7] in which multifunctional structure-power composites have been developed and investigated for use in unmanned vehicle applications. Thomas and Qidwai [4] first introduce the concept of the multifunctional structure battery in which polymer–lithium ion battery layers with structural additives are used to both store energy and support aerodynamic loads in a UAV. In a subsequent study, Thomas and Qidwai [5] provide formulations for the change in flight endurance of a UAV with an

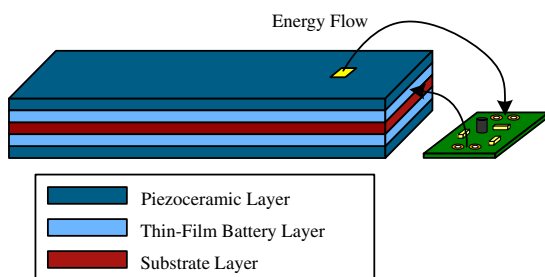
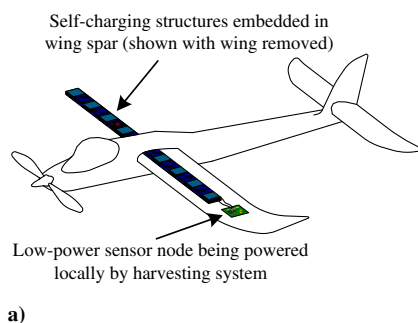


Fig. 1 Schematic of self-charging structure.



a)

integrated structure battery, and they fabricate and perform flight testing on a small flying-wing UAV, called the Wasp, which includes structure batteries integrated into the wings. More recently, Thomas and Qidwai have investigated the use of structure batteries in unmanned underwater vehicles. Qidwai et al. [6] describe the design and fabrication of structure batteries specifically developed for marine systems containing lithium–ion batteries embedded within fiber-reinforced polymer layers. Continuing the work, Rohatgi et al. [7] present the experimental evaluation of the fabricated structure batteries. The multifunctional composites are tested both mechanically via static three-point bend testing and electrically through charge/discharge cycling of the battery layers.

The authors have recently developed a multifunctional energy harvesting solution in which energy harvesting, energy storage, and load-bearing ability have been achieved in a single composite device [8]. The proposed self-charging structures contain piezoelectric layers for scavenging energy, thin-film battery layers for storing the scavenged energy, and they can be embedded into a structure to carry load. Details of the design, fabrication, modeling, and experimental evaluation of the prototype device have been given.

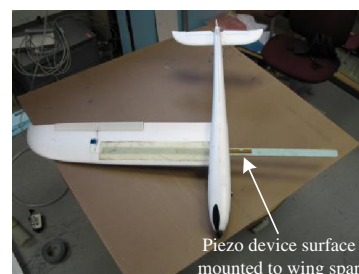
This paper extends the concept and modeling presented in [8] by applying the multifunctional philosophy to a UAV wing spar. A multifunctional wing spar for low-power vibration-based energy generation and storage is investigated. A representative aluminum spar with embedded piezoceramic and battery layers is modeled using the assumed modes method, and experimental tests are conducted on a prototype to validate the model. Finally, the simultaneous energy generation and storage ability of the multifunctional wing spar is demonstrated through charge/discharge testing under dynamic excitation.

II. Overview of Self-Charging Structures

To improve the functionality and reduce the adverse loading effects of traditional piezoelectric harvesting approaches, the authors have developed the self-charging structure design, shown in Fig. 1. Self-charging structures contain both power-generation and energy-storage capabilities in a multilayered, composite platform consisting of active piezoceramic layers for scavenging energy, thin-film battery layers for storing scavenged energy and a central metallic substrate layer arranged in a bimorph configuration. The operational principle behind the device involves simultaneous generation of electrical energy when subjected to dynamic loading causing deformations in the structure, as well as energy storage in the thin-film battery layers. Energy is transferred directly from the piezoceramic layers through appropriate conditioning circuitry to the thin-film battery layers; thus, a single device is capable of both generating and storing electrical energy. Additionally, the self-charging structures are capable of carrying loads as structural members due to the stiffness of the composite device.

III. Energy Harvesting in Unmanned Aerial Vehicles

Multifunctional self-charging structures can be embedded into the wing spar of a UAV, as shown in Fig. 2a, with the goal of providing a local power source for remote low-power wireless sensors such as



b)

Fig. 2 Small UAV a) shown schematically with embedded self-charging structures in wing spar powering low-power sensor node, and b) pictured with piezoelectric device surface mounted to wing spar.

accelerometers, structural health monitoring nodes, or even low-power imaging devices or cameras. Providing a local power source composed of both harvesting and storage elements is beneficial because it eliminates the need to run wires and tap into the propulsive power supply of the aircraft, thus reducing mass and complexity while allowing the sensors to operate wirelessly. Additionally, a multifunctional approach in which the composite harvester is embedded into the wing spar and supports structural loads in the wings is valuable because it can reduce or eliminate the added mass of the harvesting device.

Previous work by Anton and Inman has investigated the potential of piezoelectric devices to harvest energy from vibrations during UAV flight [3]. The wing spar of a small radio-control aircraft was modified to include surface mounted piezoelectric material, as shown in Fig. 2b. Flight testing results show that an average power of about $11.3 \mu\text{W}$ can be harvested during level flight from this nonoptimized design. It is expected that a multifunctional design in which the harvester is embedded into the wing spar and properly designed for maximum energy conversion will provide an increased power output.

IV. Electromechanical Modeling

An electromechanical model of an energy harvesting/energy-storage UAV wing spar is developed. The model presented in this section is based on the experimentally validated assumed modes model given by Erturk and Inman [9–11], and it extends the modeling presented by the authors in [8] by considering self-charging structures embedded into a substrate (i.e., wing spar) and the contributions of an arbitrary lumped mass (i.e., sensor node). The assumed modes method is an approximate distributed parameter modeling technique, closely related to the more common Rayleigh–Ritz method [12,13] (in fact, both methods yield identical discretized equations), that uses the extended Hamilton’s principle along with the energy expressions to derive the equations of motion of a system. Alternative ways to formulate and solve the resulting electro-mechanical problem include finite element modeling [14–16] or analytical modeling [17] with appropriate eigenfunctions.

A. Modeling Assumptions and Device Configuration

Consider the piezoelectric energy harvesting wing spar configurations shown in Fig. 3 for a half-spar model with the moving base at the clamped end representing the aircraft fuselage. The spar contains two piezoelectric layers and is symmetric about the x axis; hence, it represents a bimorph configuration. Both series (Fig. 3a) and parallel (Fig. 3b) electrode connections of the piezoelectric devices are considered. The structures are excited under translational base acceleration $a_b(t)$ imposed in the transverse direction (z direction) at the clamped end. The linearly elastic cantilevered spar is assumed to be sufficiently thin such that shear deformation and rotary inertia effects are negligible, allowing Euler–Bernoulli assumptions for small oscillations. Since the governing equations are linear, the excitation amplitude is assumed to be sufficiently low. The electrode pairs covering the piezoelectric surfaces are assumed to have negligible thickness and to be perfectly conductive such that a single electric potential can be defined across them. QuickPack® QP10n piezoelectric devices manufactured by Midé Technology, Corporation are used in the spar. Each QuickPack device contains monolithic PZT-5A bracketed by Kapton, as shown in Fig. 3. Directly following the piezoelectric layers, two thin-film battery layers are also embedded into the spar. Thinergy® MEC 101-7SES thin-film batteries manufactured by Infinite Power Solutions, Inc., are used. To prevent electrical shorting of the batteries (for which the outer substrate serves as the electrodes), a Kapton film layer is placed between the substrate and the batteries. 3M ScotchWeld™ DP460 high shear strength two-part epoxy is used to bond all layers, and all bonding layers are assumed to be perfect with identical thickness. Lastly, a sensor node is modeled as a lumped mass at an arbitrary location near the free end of the spar.

B. Energy Formulations for the Electromechanical Spar

The absolute motion of the spar is a combination of the base motion and the relative motion of the beam given by

$$w_{\text{abs}}(x, t) = w_b(t) + w_{\text{rel}}(x, t) \quad (1)$$

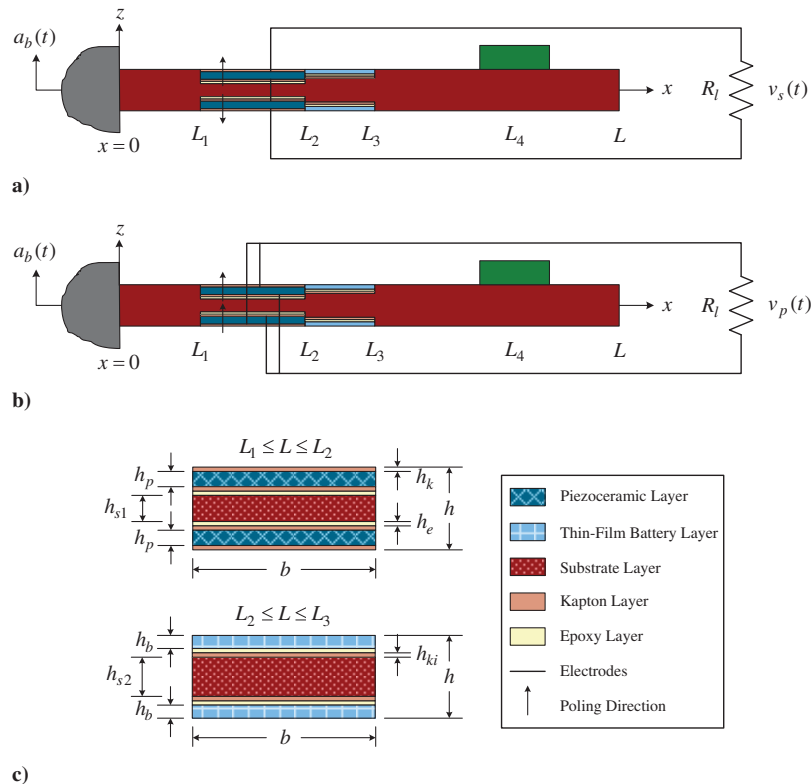


Fig. 3 Multifunctional piezoelectric energy harvesting wing spar configurations showing a) series and b) parallel connection of the piezoelectric layers along with c) cross-sectional views of both composite sections.

where w_{abs} is the absolute displacement of the beam, w_b is the base translation, and w_{rel} is the displacement of the beam relative to the moving base.

The total potential energy in the beam is given by

$$U = \frac{1}{2} \left(\int_{V_s} S_{xx} T_{xx} dV_s + \int_{V_p} S_{xx} T_{xx} dV_p \right) \quad (2)$$

where S_{xx} is the strain, T_{xx} is the stress, subscript s represents structure materials, subscript p represents piezoelectric materials, and the integrations are performed over the volume of the materials. All nonpiezoelectric layers (substrate and battery layers) are considered as structure materials.

The potential energy, or strain energy, in the structure layers (which are assumed to be linear elastic) is

$$U_s = \frac{1}{2} \int_0^L YI_s(x) \left(\frac{\partial^2 w_{\text{rel}}(x, t)}{\partial x^2} \right)^2 dx \quad (3)$$

where $YI_s(x)$ is the bending stiffness of the structure materials (Y is the elastic modulus and I is the mass moment of inertia). The bending stiffness of the nonuniform structure is given by

$$YI_s(x) = YI_s[H(L_1 - x) + H(x - L_3)] + YI_{c1}H(x - L_1)H(L_2 - x) + YI_{c2}H(x - L_2)H(L_3 - x) \quad (4)$$

where $H(x)$ is the Heaviside step function and YI_s , YI_{c1} , and YI_{c2} are the bending stiffnesses of the substrate material in the uniform sections from $0 \leq x \leq L_1$ and $L_3 \leq x \leq L$, in the first composite section from $L_1 < x < L_2$ and in the second composite section from $L_2 < x < L_3$, respectively.

The stress in the piezoelectric layers is

$$T_{xx}(x, z, t) = T_1 = c_{11}^E S_1 - e_{31} E_3 \quad (5)$$

where c_{11}^E is the elastic modulus of the piezoelectric measured at constant electric field, S_1 is the strain in the x direction (i.e., $S_1 = S_{xx}$), e_{31} is the piezoelectric stress constant, and E_3 is the electric field across the electrodes of the piezoelectric layers (note that $e_{31} = d_{31}/s_{11}^E$, where d_{31} is the piezoelectric strain constant and $s_{11}^E = 1/c_{11}^E$ is the elastic compliance of the piezoelectric layer measured at constant electric field). The electric field can be expressed in terms of the voltage output of the piezoelectric layers; however, the expressions will differ between the series and parallel connection cases. From this point on, separate formulations for the series and parallel electrode connections must be given.

The total potential energy in the piezoelectric layers is the sum of the potential energy in the top and bottom layers, which are assumed to be identical and symmetric, resulting in

$$U_p^s = \int_{L_1}^{L_2} \left(c_{11}^E I_p \left(\frac{\partial^2 w_{\text{rel}}(x, t)}{\partial x^2} \right)^2 - J_p^s v_s(t) \frac{\partial^2 w_{\text{rel}}(x, t)}{\partial x^2} \right) dx \quad (6)$$

$$U_p^p = \int_{L_1}^{L_2} \left(c_{11}^E I_p \left(\frac{\partial^2 w_{\text{rel}}(x, t)}{\partial x^2} \right)^2 - J_p^p v_p(t) \frac{\partial^2 w_{\text{rel}}(x, t)}{\partial x^2} \right) dx \quad (7)$$

where superscripts s and p stand for series and parallel connections of the piezoelectric layers, $c_{11}^E I_p$ is the bending stiffness of the piezoelectric layer, and the piezoelectric coupling terms are

$$J_p^s = \iint_p \frac{e_{31}}{2h_p} z dy dz \quad (8)$$

$$J_p^p = \iint_p \frac{e_{31}}{h_p} z dy dz \quad (9)$$

where the integrals are evaluated over the domain of the piezoelectric layers. The total potential energy of the structure can be written by summing the potential energy in the piezoelectric layers and the strain energy of the structure layers.

The total kinetic energy of the beam is

$$T_{\text{beam}} = \frac{1}{2} \left(\int_{V_s} \rho_s \left(\frac{\partial w(x, t)}{\partial t} \right)^2 dV_s + \int_{V_p} \rho_p \left(\frac{\partial w(x, t)}{\partial t} \right)^2 dV_p \right) \quad (10)$$

which can be rewritten as

$$T_{\text{beam}} = \frac{1}{2} \int_0^L (\rho A_s(x) + \rho A_p(x)) \left[\left(\frac{\partial w_b(t)}{\partial t} \right)^2 + 2 \frac{\partial w_b(t)}{\partial t} \frac{\partial w_{\text{rel}}(x, t)}{\partial t} + \left(\frac{\partial w_{\text{rel}}(x, t)}{\partial t} \right)^2 \right] dx \quad (11)$$

where $\rho A_s(x)$ and $\rho A_p(x)$ are the spatially dependent mass density functions of the structure and piezoelectric layers given by

$$\rho A_s(x) = \rho A_s[H(L_1 - x) + H(x - L_3)] + \rho A_{c1}H(x - L_1)H(L_2 - x) + \rho A_{c2}H(x - L_2)H(L_3 - x) \quad (12)$$

$$\rho A_p(x) = \rho A_p H(x - L_1)H(L_2 - x) \quad (13)$$

where ρA_s , ρA_{c1} , and ρA_{c2} are the mass densities of the substrate material in the uniform sections from $0 \leq x \leq L_1$ and $L_3 \leq x \leq L$, in the first composite section from $L_1 < x < L_2$ and in the second composite section from $L_2 < x < L_3$, respectively, and ρA_p is the mass density of the piezoelectric layers in the first composite section from $L_1 < x < L_2$.

The kinetic energy of the lumped mass (i.e., sensor node) is given by

$$T_{\text{mass}} = \frac{1}{2} M \left[\left(\frac{\partial w_b(t)}{\partial t} \right)^2 + 2 \frac{\partial w_b(t)}{\partial t} \frac{\partial w_{\text{rel}}(L_4, t)}{\partial t} + \left(\frac{\partial w_{\text{rel}}(L_4, t)}{\partial t} \right)^2 \right] \quad (14)$$

where M is the mass of the lumped mass. The total kinetic energy of the system can be expressed as the sum of the kinetic energy of the beam and the kinetic energy of the lumped mass.

The internal electrical energy in the piezoelectric layers is given by

$$W_{\text{ie}} = \frac{1}{2} \int_{V_p} E_3 D_3 dV_p \quad (15)$$

The electric displacement D_3 in the piezoelectric layers is

$$D_3 = e_{31} S_1 + \varepsilon_{33}^S E_3 \quad (16)$$

where ε_{33}^S is the dielectric permittivity of the piezoelectric measured at constant strain (denoted by the superscript S). The total internal electrical energy in the piezoelectric layers is the sum of the electrical energy in the top and bottom layers. Because of the symmetry of the identical piezoelectric layers, the internal electric energy can be written as

$$W_{\text{ie}}^s = \frac{1}{2} \int_{L_1}^{L_2} 2J_p^s v_s(t) \frac{\partial^2 w_{\text{rel}}(x, t)}{\partial x^2} dx + \frac{1}{4} C_p v_s^2(t) \quad (17)$$

$$W_{\text{ie}}^p = \frac{1}{2} \int_{L_1}^{L_2} 2J_p^p v_p(t) \frac{\partial^2 w_{\text{rel}}(x, t)}{\partial x^2} dx + C_p v_p^2(t) \quad (18)$$

where the internal capacitance of a piezoelectric layer C_p is given by

$$C_p = \varepsilon_{33}^S \frac{A_p}{h_p} \quad (19)$$

where A_p is the electrode area.

The effects of base excitation are considered in the kinetic energy term, and mechanical damping is to be introduced later in the form of

proportional damping; therefore, the only nonconservative virtual work is due to the piezoelectric charge output, giving

$$\delta W_{\text{ncc}} = Q(t)\delta v(t) \quad (20)$$

where $Q(t)$ is the electric charge output of the piezoelectric layers.

C. Substitution of the Assumed Solution

The assumed modes method involves discretization of the energy expressions by substitution of an assumed series solution for the unknown relative beam displacement composed of kinematically admissible functions (or trial functions) $\phi_r(x)$ multiplied by generalized (or modal) coordinates $\eta_r(t)$ of the form

$$w_{\text{rel}}(x, t) = \sum_{r=1}^N \phi_r(x)\eta_r(t) \quad (21)$$

where N number of modes are used in the summation. The admissible functions must satisfy the geometric boundary conditions. A simple admissible function satisfying the essential boundary conditions of a clamped-free thin beam is [18]

$$\phi_r(x) = 1 - \cos\left(\frac{(2r-1)\pi x}{2L}\right) \quad (22)$$

Substitution of the assumed solution [Eq. (21)] into the potential energy expressions [Eqs. (3), (6), and (7)], kinetic energy expressions [Eqs. (11) and (14)], and internal electrical energy expressions [Eqs. (17) and (18)] leads to

$$U^s = \frac{1}{2} \sum_{r=1}^N \sum_{l=1}^N (\eta_r(t)\eta_l(t)k_{rl} - 2\eta_r(t)v_s(t)\theta_r^s) \quad (23)$$

$$U^p = \frac{1}{2} \sum_{r=1}^N \sum_{l=1}^N (\eta_r(t)\eta_l(t)k_{rl} - 2\eta_r(t)v_p(t)\theta_r^p) \quad (24)$$

$$T = \frac{1}{2} \sum_{r=1}^N \sum_{l=1}^N (\dot{\eta}_r(t)\dot{\eta}_l(t)m_{rl} + 2\dot{\eta}_r(t)p_r) + \frac{1}{2} \int_0^L (\rho A_s(x) + \rho A_p(x)) \left(\frac{\partial w_b(t)}{\partial t}\right)^2 dx + \frac{1}{2} M \left(\frac{\partial w_b(t)}{\partial t}\right)^2 \quad (25)$$

$$W_{\text{ie}}^s = \frac{1}{2} \sum_{r=1}^N \left(2\eta_r(t)v_s(t)\theta_r^s + \frac{1}{2} C_p v_s^2(t)\right) \quad (26)$$

$$W_{\text{ie}}^p = \frac{1}{2} \sum_{r=1}^N \left(2\eta_r(t)v_p(t)\theta_r^p + 2C_p v_p^2(t)\right) \quad (27)$$

where

$$k_{rl} = \int_0^L YI_s(x)\phi_r''(x)\phi_l''(x) dx + 2 \int_{L_1}^{L_2} c_{11}^E I_p \phi_r''(x)\phi_l''(x) dx \quad (28)$$

$$\theta_r^s = \int_{L_1}^{L_2} J_p^s \phi_r''(x) dx \quad (29)$$

$$\theta_r^p = \int_{L_1}^{L_2} J_p^p \phi_r''(x) dx \quad (30)$$

$$m_{rl} = \int_0^L (\rho A_s(x) + \rho A_p(x))\phi_r(x)\phi_l(x) dx + M\phi_r(L_4)\phi_l(L_4) \quad (31)$$

$$p_r = \int_0^L (\rho A_s(x) + \rho A_p(x))\phi_r(x) \frac{\partial w_b(t)}{\partial t} dx + M\phi_r(L_4) \frac{\partial w_b(t)}{\partial t} \quad (32)$$

where prime represents ordinary differentiation with respect to the spatial variable x , and an overdot represents ordinary differentiation with respect to the temporal variable t .

D. Lagrange Equations with Electromechanical Coupling

The extended Hamilton's principle for electromechanical systems is [19]

$$\int_{t_1}^{t_2} (\delta T - \delta U + \delta W_{\text{ie}} + \delta W_{\text{ncc}}) dt = 0 \quad (33)$$

where δT , δU , and δW_{ie} are the first variations of the kinetic energy, potential energy, and internal electrical energy; and δW_{ncc} is the virtual work of all nonconservative forces. Based on the extended Hamilton's principle, the electromechanical Lagrange equations are

$$\frac{d}{dt} \left(\frac{\partial T}{\partial \dot{\eta}_i} \right) - \frac{\partial T}{\partial \eta_i} + \frac{\partial U}{\partial \eta_i} - \frac{\partial W_{\text{ie}}}{\partial \eta_i} = 0 \quad (34)$$

$$\frac{d}{dt} \left(\frac{\partial T}{\partial \dot{v}_i} \right) - \frac{\partial T}{\partial v_i} + \frac{\partial U}{\partial v_i} - \frac{\partial W_{\text{ie}}}{\partial v_i} = Q \quad (35)$$

where Q is the electric charge output resulting from the nonconservative virtual electrical work δW_{ncc} .

Equation (34) leads to the first set of Lagrange equations given by

$$\sum_{l=1}^N (m_{il}\ddot{\eta}_l + k_{il}\eta_l - 2\theta_l^s v_s - f_i) = 0 \quad (\text{series connection}) \quad (36)$$

$$\sum_{l=1}^N (m_{il}\ddot{\eta}_l + k_{il}\eta_l - 2\theta_l^p v_p - f_i) = 0 \quad (\text{parallel connection}) \quad (37)$$

where f_i is the forcing due to base excitation given by

$$f_i = -\frac{\partial p_i}{\partial t} = -\int_0^L (\rho A_s(x) + \rho A_p(x))\phi_i(x) \frac{\partial^2 w_b(t)}{\partial t^2} dx + M\phi_i(L_4) \frac{\partial^2 w_b(t)}{\partial t^2} \quad (38)$$

Equation (35) yields the second set of Lagrange equations as

$$\frac{1}{2} C_p \dot{v}_s + \frac{v_s}{R_l} + \sum_{r=1}^N (2\dot{\eta}_r \theta_r^s) = 0 \quad (\text{series connection}) \quad (39)$$

$$2C_p \dot{v}_p + \frac{v_p}{R_l} + \sum_{r=1}^N (2\dot{\eta}_r \theta_r^p) = 0 \quad (\text{parallel connection}) \quad (40)$$

where the temporal derivative has been taken and the time rate of change of the electrical charge output \dot{Q} has been replaced by the electrical current passing through the load resistor, which is equivalent to v/R_l .

E. Equivalent Series/Parallel Representation of the Lagrange Equation

At this point, it is convenient to introduce an equivalent representation of the electromechanical Lagrange equations for the series and parallel cases, as suggested by Erturk and Inman [11], in which a single formulation with modified electromechanical coupling and capacitance terms is used. Observe that the only differences in the coupled Lagrange equations between the series and parallel electrode connection cases involve the electromechanical coupling terms (i.e.,

θ_i) and the capacitance terms. Considering these differences, one can define the following equivalent Lagrange equations:

$$\sum_{i=1}^N (m_{ii}\ddot{\eta}_i + k_{ii}\eta_i - \theta_i^{\text{eq}}v - f_i) = 0 \quad (41)$$

$$C_p^{\text{eq}}\dot{v} + \frac{v}{R_l} + \sum_{r=1}^N (\dot{\eta}_r \theta_r^{\text{eq}}) = 0 \quad (42)$$

where the equivalent electromechanical coupling θ^{eq} and capacitance C_p^{eq} are selected from Table 1 depending on whether a series or parallel solution is desired, and where the piezoelectric coupling term J_p is given by

$$J_p = \iint_p \frac{e_{31}}{h_p} z \, dy \, dz \quad (43)$$

F. Solution of the Equivalent Representation of the Lagrange Equations

Rewriting the equivalent Lagrange equations given by Eqs. (41) and (42) in matrix form and introducing proportional damping to the first equation gives

$$[\mathbf{M}]\ddot{\boldsymbol{\eta}} + [\mathbf{C}]\dot{\boldsymbol{\eta}} + [\mathbf{K}]\boldsymbol{\eta} - \boldsymbol{\Theta}^{\text{eq}}v = \mathbf{f} \quad (44)$$

$$C_p^{\text{eq}}\dot{v} + \frac{v}{R_l} + \boldsymbol{\Theta}^{\text{eq}T}\dot{\boldsymbol{\eta}} = 0 \quad (45)$$

where superscript T represents the matrix transpose; the mass, stiffness, and damping matrices ($[\mathbf{M}]$, $[\mathbf{K}]$, and $[\mathbf{C}]$) are $N \times N$; the generalized coordinates $\boldsymbol{\eta}$, the forcing vector \mathbf{f} , and the electromechanical coupling vector $\boldsymbol{\Theta}^{\text{eq}}$ are $N \times 1$; and the damping matrix is given by

$$[\mathbf{C}] = \alpha[\mathbf{M}] + \beta[\mathbf{K}] \quad (46)$$

where α and β are constants of proportionality.

Assuming harmonic base excitation at a frequency ω of the form $w_b(t) = w_b e^{j\omega t}$, which leads to a base acceleration of $a_b e^{j\omega t}$ (where $a_b = -\omega^2 w_b$), the forcing vector as well as the solution for the generalized coordinate and voltage response become harmonic of the form

$$\mathbf{f} = \mathbf{F} e^{j\omega t} \quad (47)$$

$$\boldsymbol{\eta} = \boldsymbol{\eta} e^{j\omega t} \quad (48)$$

$$v = V e^{j\omega t} \quad (49)$$

Substitution of these assumed solutions into the matrix equations [Eqs. (44) and (45)] and solving simultaneously for the voltage response $v(t)$ and displacement response [recalling Eq. (21)] $w_{\text{rel}}(x, t)$, the following voltage-to-base acceleration and displacement-to-base acceleration frequency response functions (FRFs) can be written:

Table 1 Equivalent electromechanical coupling and capacitance terms for series and parallel electrode connections (from Erturk and Inman [11])

	Series connection	Parallel connection
θ_i^{eq}	$\int_{L_1}^{L_2} J_p \phi_i''(x) \, dx$	$2 \int_{L_1}^{L_2} J_p \phi_i''(x) \, dx$
C_p^{eq}	$\frac{1}{2} C_p$	$2 C_p$

$$\frac{v(t)}{a_b e^{j\omega t}} = -j\omega \left(j\omega C_p^{\text{eq}} + \frac{1}{R_l} \right)^{-1} \boldsymbol{\Theta}^{\text{eq}T} \left(-\omega^2 [\mathbf{M}] + j\omega [\mathbf{C}] + [\mathbf{K}] \right. \\ \left. + j\omega \left(j\omega C_p^{\text{eq}} + \frac{1}{R_l} \right)^{-1} \boldsymbol{\Theta}^{\text{eq}} \boldsymbol{\Theta}^{\text{eq}T} \right)^{-1} \tilde{\mathbf{F}} \quad (50)$$

$$\frac{w_{\text{rel}}(x, t)}{a_b e^{j\omega t}} = \boldsymbol{\Phi}^T(x) \left(-\omega^2 [\mathbf{M}] + j\omega [\mathbf{C}] + [\mathbf{K}] \right. \\ \left. + j\omega \left(j\omega C_p^{\text{eq}} + \frac{1}{R_l} \right)^{-1} \boldsymbol{\Theta}^{\text{eq}} \boldsymbol{\Theta}^{\text{eq}T} \right)^{-1} \tilde{\mathbf{F}} \quad (51)$$

where the components of the forcing vector are given by

$$\tilde{F}_i = - \left(\int_0^L (\rho A_s(x) + \rho A_p(x)) \phi_i(x) \, dx + M \phi_i(L_4) \right) \quad (52)$$

V. Experimental Validation of the Assumed Modes Formulation

A representative wing spar with embedded piezoelectric and thin-film battery layers is fabricated and experimentally tested, and the results are compared with the model predictions.

A. Experimental Setup

A thin 3003-H14 aluminum alloy beam is selected as the substrate layer of the representative wing spar. Two opposite faces of the beam are machined to allow bonding of the piezoelectric and thin-film battery layers on the symmetric structure. QuickPack QP10n piezoelectric devices are bonded near the root of the beam, and Thinergy MEC 101-7SES thin-film batteries are bonded just after the piezoelectric layers. The Thinergy batteries have a rated voltage of 4.0 V and a capacity of 0.7 mAh. Geometric and material properties of the substrate, piezoelectric, and battery layers are given in Table 2. It should be noted that the QP10n device contains an active PZT-5A element bracketed in Kapton; hence, both the dimensions of the full device as well as the active element are given in Table 2. The piezoelectric material properties are taken from the manufacturer's datasheet (QP10n uses 3195HD piezoelectric material from CTS Corporation),[§] where the battery properties are found from experimental tests and measurements. The mass density of the battery is found by simply measuring its volume and mass, where the elastic modulus is found by fitting a distributed parameter bending beam model to experimental FRF data obtained with a battery mounted in a cantilever configuration and subjected to base excitation. The elastic moduli of the Kapton layers and epoxy layers are taken as 3.7 and 3 GPa, respectively, and the mass densities are taken as 1233 and 1000 kg/m³, respectively [20].

The device is clamped to an APS Dynamics, Inc., 113 long-stroke shaker, which is powered by an APS Dynamics, Inc., 125 power amplifier, with an overhang length of 25.40 cm, as shown in Fig. 4a. In the clamped configuration, the device becomes a five-segment beam with an initial 25.40 mm segment containing only the aluminum substrate, followed by a 9.53 mm transition section containing only the reduced thickness substrate to allow for the electrode connection of the QP10n device, a 50.80 mm composite section containing the substrate layer and symmetric piezoelectric layers bonded with epoxy to the substrate, a 25.40 mm composite section containing the substrate and symmetric thin-film battery layers insulated with Kapton and bonded with epoxy, and finally a 142.88 mm segment, which again contains only the aluminum substrate. A 15.6 g lumped mass in the form of two rectangular magnets of dimension 25.4 × 6.35 × 6.35 mm placed on opposite faces of the beam is fixed at a distance of 203.2 mm from the root of the beam. A DSP Technology, Inc., SigLab 20-42 data acquisition system is used for all FRF measurements. Low-amplitude chirp

[§]Data available at http://www.mide.com/pdfs/quickpack_specs_piezo_properties.pdf [retrieved 2 March 2011].

Table 2 Geometric and material properties of self-charging structure components

Property	Aluminum substrate	Quickpack QP10n overall device	Quickpack QP10n active element	Thinergy MEC 101-7SES
Length, mm	304.8	50.8	45.97	25.4
Width, mm	26.62	25.4	20.574	25.4
Thickness, mm	3.237	0.381	0.254	0.178
Elastic modulus, GPa	69	—	67	55
Mass density, kg/m ³	2730	—	7800	4000
Piezoelectric strain constant d_{31} , pC/N	—	—	-190	—
Dielectric permittivity constant ϵ_{33}^s , pF/m	—	—	14.6	—

signals are used to excite the shaker, and 5 averages are taken for each measurement. The input acceleration is measured using a PCB Piezotronics, Inc., U352C67 accelerometer attached to the base of the clamp with wax, the tip velocity is measured using a Polytec, Inc., PDV-100 laser Doppler vibrometer by placing a small piece of retroreflective tape at the tip of the cantilever, and the voltage output of the piezoelectric layers is measured directly with the SigLab data acquisition system using an Agilent Technologies, Inc., N2862A 10:1 probe. Two frequency response functions are therefore measured: the tip velocity-to-base acceleration FRF and the voltage-to-base acceleration FRF. The overall test setup is shown in Fig. 4b. It is worth noting that the laser vibrometer measures the absolute tip velocity of the beam as opposed to the relative tip displacement that is predicted by Eq. (51); however, Eq. (51) leads to the following expression for the absolute tip velocity FRF:

$$\frac{V_{\text{abs}}(L, t)}{a_b e^{j\omega t}} = \frac{1}{j\omega} + j\omega \Phi^T(L) \left(-\omega^2 [\mathbf{M}] + j\omega [\mathbf{C}] + [\mathbf{K}] + j\omega \left(j\omega C_p^{\text{eq}} + \frac{1}{R_l} \right)^{-1} \Theta^{\text{eq}} \Theta^{\text{eq}T} \right)^{-1} \tilde{\mathbf{F}} \quad (53)$$

B. Experimental Results

Experimental tip velocity-to-base acceleration and voltage-to-base acceleration FRFs measured for both the series and parallel connections of the electrodes for a set of load resistances ranging

from 100 Ω to 1 M Ω are shown in Figs. 5 and 6, respectively (where the base acceleration is given in terms of the acceleration of gravity $g = 9.81 \text{ m/s}^2$). The tip velocity and voltage FRFs are predicted using Eqs. (53) and (50), respectively, and plotted over the experimental results in Figs. 5 and 6. Forty modes are used in the assumed modes formulation ($N = 40$) to ensure the convergence of the fundamental natural frequency using the admissible functions given by Eq. (22). From the results, it is clear that the model accurately predicts the coupled electrical and mechanical response of the structure. As the load resistance increases from 100 Ω (near the short-circuit condition) to 1 M Ω (near the open-circuit condition), the experimentally measured fundamental natural frequency shifts from 28.13 to 28.38 Hz for both series and parallel connection cases. These frequencies are predicted by the assumed modes formulation as 28.10 and 28.40 Hz, respectively. The model predictions of the magnitude of the FRFs are also well matched. The experimental voltage FRFs show a maximum peak voltage output (obtained for the largest load resistance) of 968.1 V/g for the series connection and 674.1 V/g for the parallel connection. It should be noted, however, that these measurements are frequency response-based linear estimates obtained from low-amplitude chirp excitation, and they are not necessarily accurate for large-amplitude excitations with nonlinear response characteristics. It is expected that the linear predictions should overestimate the mechanical and electrical response amplitudes, and hence provide an upper bound due to ignoring the nonlinear piezoelectric effects as well as dissipative nonlinearities [21,22]. The maximum tip velocity for the short-circuit

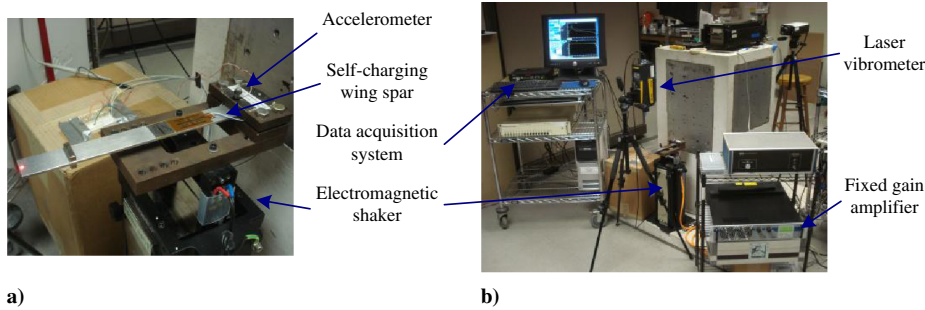


Fig. 4 Experimental setup showing a) wing spar clamped to shaker, and b) overall setup.

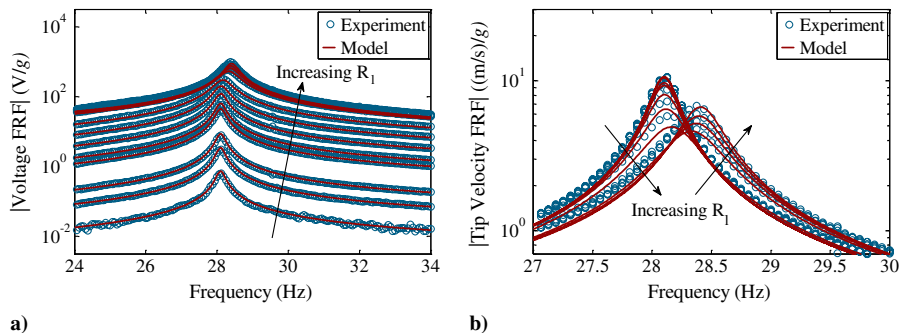


Fig. 5 Experimental and numerical a) tip velocity-to-base acceleration FRFs and b) voltage-to-base acceleration FRFs for series electrode connection case for various load resistances.

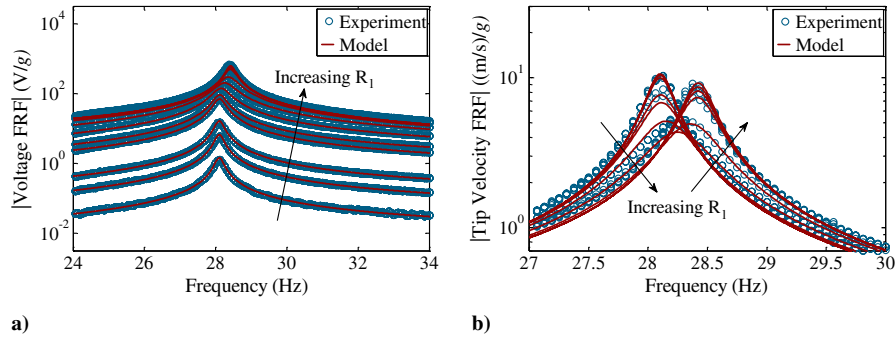


Fig. 6 Experimental and numerical a) tip velocity-to-base acceleration FRFs and b) voltage-to-base acceleration FRFs for parallel electrode connection case for various load resistances.

condition is measured experimentally as 10.57 and 10.30 (m/s)/g for the series and parallel cases, respectively, and is predicted by the model as 10.64 and 10.59 (m/s)/g. For the open-circuit condition, maximum tip velocities of 6.83 and 9.15 (m/s)/g are measured for the series and parallel cases, respectively, and the predicted values are 6.67 and 9.21 (m/s)/g.

Based on the voltage FRFs given in Figs. 5a and 6a, several electrical performance curves can be extracted to better describe the electrical behavior of the system. The variation of the peak voltage, current, and electrical power with load resistance can be determined

at both the short-circuit and open-circuit resonance frequencies, which are of particular importance for energy harvesting purposes as they provide bounds on the fundamental resonance frequency of the system under examination. For any load resistance, the fundamental natural frequency will lie between the short-circuit and open-circuit resonance frequencies. The variation of the peak voltage with load resistance is presented in Figs. 7a and 7b for the series and parallel electrode connections, respectively. The model predictions are in good agreement with the experimental data. The peak voltage output values predicted by the model for the largest load resistance at the

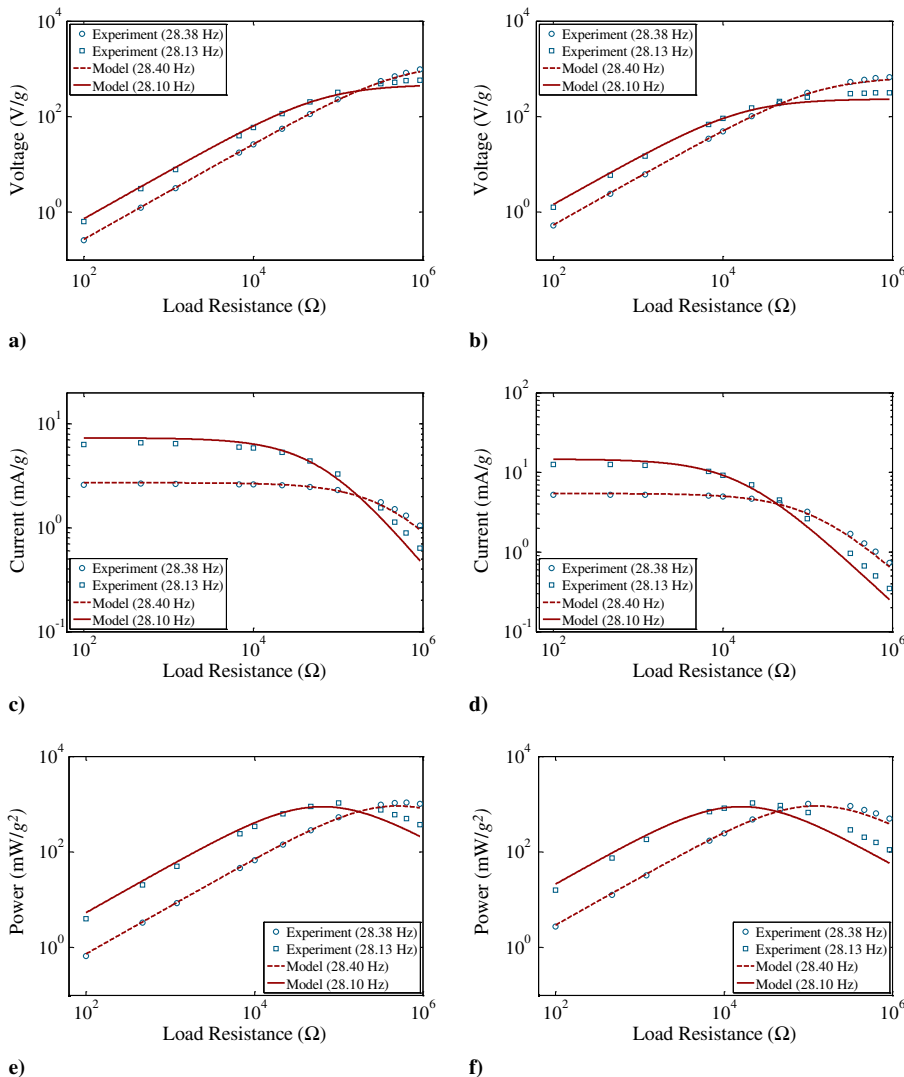


Fig. 7 Experimental and numerical electrical performance curves for peak voltage output in a) series and b) parallel cases, current output in c) series and d) parallel cases, and power output in e) series and f) parallel cases with varying load resistance.

short-circuit and open-circuit resonance frequencies are 439.5 and 875.0 V/g, respectively, for the series case and 593.9 and 230.4 V/g, respectively, for the parallel case.

Figures 7c and 7d show the variation of the peak current output with load resistance for the series and parallel electrode connection cases, respectively. The peak current output is predicted by the model for the smallest load resistance at the short-circuit and open-circuit resonance frequencies as 7.32 and 2.71 mA/g, respectively, for the series case and 14.58 and 5.42 mA/g, respectively, for the parallel case.

Lastly, the variation of the power output with load resistance is given in Figs. 7e and 7f for the series and parallel cases, respectively. For both cases, a peak power output exists for each excitation frequency at different optimal load resistance values between short-circuit and open-circuit conditions. Additionally, the peak power output for the short-circuit and open-circuit conditions are roughly equal. Furthermore, the peak powers predicted for the series connection and parallel connection are identical. The peak power output for excitation at the short-circuit resonance frequency is predicted by the model as 884.9 mW/g² for a load resistance of 64.04 k Ω for the series connection and 16.09 k Ω for the parallel connection. For excitation at the open-circuit resonance frequency, the model predicts a peak power output of 913.9 mW/g² for a load resistance of 503.3 k Ω for the series connection and 126.1 k Ω for the parallel connection. Again, these peak values are linear estimates based on low-amplitude chirp excitation FRFs and are not necessarily accurate for large-amplitude excitation.

VI. Experimental Demonstration of the Self-Charging Concept

Charge/discharge experiments are conducted in which the device is first excited at resonance with the piezoelectric layers connected to charge a battery layer while the voltage of and current flowing into the thin-film battery layer are monitored. Subsequently, the thin-film battery is discharged while monitoring battery current and voltage. Charge and discharge profiles can then be defined.

Using the same experimental setup shown in Fig. 4a, the cantilever spar is excited at resonance with the piezoelectric layers and a single battery layer connected to a simple linear voltage regulator energy harvesting circuit, shown schematically in Fig. 8. A Keithley Instruments, Inc., 2611A SourceMeter is used for the current measurements in charging and for both current and voltage measurements in discharging. In charging, a National Instruments Corporation (NI) CompactDAQ chassis using a NI 9215 four-channel analog voltage input card is used to measure the battery voltage. Additionally, a NI 9233 four-channel analog input card with integrated electronic piezoelectric coupling is used to measure the base acceleration input, and a NI 9263 four-channel analog output card is used to excite the shaker. For this experimentation, the two piezoelectric layers of the self-charging spar are connected in parallel for increased current output and used to charge a single battery layer. The base excitation amplitude is selected based on previous flight testing results that show acceleration amplitudes around ± 1.0 g [3]. Considering that the excitation frequency experienced on the aircraft does not match the resonance of the harvester and, in fact, varies throughout flight, an acceleration level of ± 0.25 g is chosen; however, the resonance tests performed here will likely still overestimate the harvesting ability of the spar during flight. The device is excited at resonance for 1 h, and the battery voltage and current into the battery are measured throughout the test. Once the test is complete, the battery is discharged using the Keithley SourceMeter. Results from both the charge and discharge tests are shown in Fig. 9. From Fig. 9a, it can be seen that the piezoelectric layers are able to supply an average of about 0.37 mA of current into the battery. Integrating the charge current over time, the capacity during charging is found to be 0.362 mAh. The discharge test results presented in Fig. 9b, show that a constant current of 1.4 mA (which corresponds to a discharge rate of twice the rated battery capacity, or 2C) is drawn from the battery throughout the test. In discharging, a capacity of 0.362 mAh is also calculated. The results of the charge/discharge testing show the ability of the multifunctional spar to operate in a self-charging manner and give an estimate of the power that can be harvested by the prototype spar. The average regulated power output of the spar

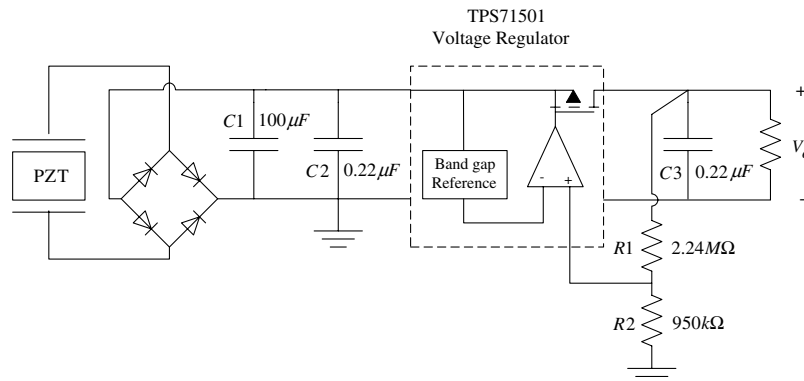


Fig. 8 Linear voltage regulator energy harvesting circuit (PZT denotes piezoelectric transducer).

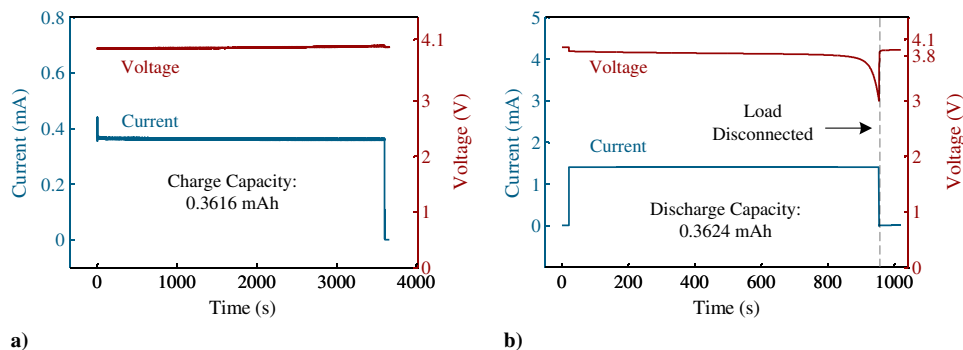


Fig. 9 Experimental curves for self-charging structures in a) charging and b) discharging under ± 0.25 g acceleration at 28.38 Hz.

during testing is around 1.5 mW, which is a reasonable value for piezoelectric energy harvesting, where typical harvested powers are in the microwatt to milliwatt range [1]. Additionally, this power level is adequate for powering various low-power electronic devices.

VII. Conclusions

Piezoelectric vibration energy harvesting in UAVs has recently attracted interest in the research community, and the development of multifunctional harvesting solutions proves beneficial for applications in which added mass and volume are critical. This paper presents the electromechanical modeling and experimental evaluation of a multifunctional composite energy harvesting wing spar for a small UAV including embedded piezoelectrics for energy generation and thin-film batteries for energy storage. The assumed modes method is employed to model the wing spar in a cantilevered configuration, and expressions for the relative displacement-to-base acceleration and voltage-to-base acceleration frequency response functions are given. Both series and parallel electrode connections of the two piezoelectric layers in the symmetric bimorph energy harvesting spar are considered. Experimental tests are conducted on a representative prototype wing spar consisting of an aluminum beam with embedded piezoelectric and thin-film battery layers in addition to a lumped mass at an arbitrary location, which represents a sensor node to be powered by the harvesting system. Model predictions are compared with experimentally measured FRFs, and good correlation between the model and experiments is found, thus verifying the model. Experiments are also conducted in which the spar is excited harmonically while the piezoelectric layers are used to charge a battery layer in order to evaluate the ability of the spar to simultaneously harvest and store energy. For an input base acceleration level of $\pm 0.25 g$ at 28.4 Hz, 1.5 mW of regulated dc power is delivered from the piezoelectric layers to the thin-film battery, corresponding to a stored capacity of 0.362 mAh in 1 h. Results of the charge/discharge testing prove the ability of the multifunctional wing spar to operate in a self-charging manner.

Acknowledgment

The authors gratefully acknowledge the support of the U.S. Air Force Office of Scientific Research Multidisciplinary University Research Initiative under grant number F9550-06-1-0326, titled Energy Harvesting and Storage Systems for Future Air Force Vehicles, and monitored by B. L. Lee.

References

- [1] Anton, S. R., and Sodano, H. A., "A Review of Power Harvesting Using Piezoelectric Materials (2003–2006)," *Smart Materials and Structures*, Vol. 16, No. 3, 2007, pp. R1–R21. doi:10.1088/0964-1726/16/3/R01
- [2] Cook-Chennault, K. A., Thambi, N., and Sastry, A. M., "Powering MEMS Portable Devices: A Review of Non-Regenerative and Regenerative Power Supply Systems with Special Emphasis on Piezoelectric Energy Harvesting Systems," *Smart Materials and Structures*, Vol. 17, No. 4, 2008, Paper 043001. doi:10.1088/0964-1726/17/4/043001
- [3] Anton, S. R., and Inman, D. J., "Vibration Energy Harvesting for Unmanned Aerial Vehicles," *Proceedings of SPIE*, Vol. 6928, 2008, Paper 692824. doi:10.1117/12.774990
- [4] Thomas, J. P., and Qidwai, M. A., "Mechanical Design and Performance of Composite Multifunctional Materials," *Acta Materialia*, Vol. 52, No. 8, 2004, pp. 2155–2164. doi:10.1016/j.actamat.2004.01.007
- [5] Thomas, J. P., and Qidwai, M. A., "The Design and Application of Multifunctional Structure-Battery Materials Systems," *JOM*, Vol. 57, No. 3, 2005, pp. 18–24. doi:10.1007/s11837-005-0228-5
- [6] Qidwai, M. A. S., Pogue, W. R., III, Thomas, J. P., and Rohatgi, A., "Design and Fabrication of Multifunctional Structure-Power Composites for Marine Applications," *Proceedings of the ASME 2008 International Mechanical Engineering Congress and Exposition*, Boston, MA, Vol. 12, American Soc. of Mechanical Engineers, Fairfield, NJ, 2008, pp. 385–393.
- [7] Rohatgi, A., Thomas, J. P., Qidwai, M. A. S., and Pogue, W. R., III, "Performance Characterization of Multifunctional Structure-Battery Composites for Marine Applications," *Proceedings of the ASME 2008 International Mechanical Engineering Congress and Exposition*, Boston, MA, Vol. 12, American Soc. of Mechanical Engineers, Fairfield, NJ, 2008, pp. 375–383.
- [8] Anton, S. R., Erturk, A., and Inman, D. J., "Multifunctional Self-Charging Structures Using Piezoceramics and Thin-Film Batteries," *Smart Materials and Structures*, Vol. 19, No. 11, 2010, Paper 115021. doi:10.1088/0964-1726/19/11/115021
- [9] Erturk, A., "Electromechanical Modeling of Piezoelectric Energy Harvesters," Ph.D. Dissertation, Virginia Polytechnic Inst. and State Univ., Blacksburg, VA, 2009.
- [10] Erturk, A., and Inman, D. J., "Assumed-Modes Formulation of Piezoelectric Energy Harvesters: Euler–Bernoulli, Rayleigh and Timoshenko Models with Axial Deformations," *Proceedings of the ASME 2010 ESDA 10th Biennial Conference on Engineering Systems, Design and Analysis*, Istanbul, Turkey, American Soc. of Mechanical Engineers, Fairfield, NJ, July 2010, pp. 405–414.
- [11] Erturk, A., and Inman, D. J., *Piezoelectric Energy Harvesting*, Wiley, New York, 2011, pp. 65–67.
- [12] duToit, N. E., and Wardle, B. L., "Experimental verification of models for microfabricated piezoelectric vibration energy harvesters," *AIAA Journal*, Vol. 45, No. 5, 2007, pp. 1126–1137. doi:10.2514/1.25047
- [13] Elvin, N. G., and Elvin, A. A., "A General Equivalent Circuit Model for Piezoelectric Generators," *Journal of Intelligent Material Systems and Structures*, Vol. 20, No. 1, 2009, pp. 3–9. doi:10.1177/1045389X08089957
- [14] Rupp, C. J., Evgrafov, A., Maute, K., and Dunn, M. L., "Design of Piezoelectric Energy Harvesting Systems: A Topology Optimization Approach Based on Multilayer Plates and Shells," *Journal of Intelligent Material Systems and Structures*, Vol. 20, No. 16, 2009, pp. 1923–1939. doi:10.1177/1045389X09341200
- [15] Yang, Y., and Tang, L., "Equivalent Circuit Modeling of Piezoelectric Energy Harvesters," *Journal of Intelligent Material Systems and Structures*, Vol. 20, No. 18, 2009, pp. 2223–2235. doi:10.1177/1045389X09351757
- [16] De Marqui, C., Jr., Erturk, A., and Inman, D. J., "An Electromechanical Finite Element Model for Piezoelectric Energy Harvester Plates," *Journal of Sound and Vibration*, Vol. 327, Nos. 1–2, 2009, pp. 9–25. doi:10.1016/j.jsv.2009.05.015
- [17] Erturk, A., and Inman, D. J., "An Experimentally Validated Bimorph Cantilever Model for Piezoelectric Energy Harvesting from Base Excitations," *Smart Materials and Structures*, Vol. 18, No. 2, 2009, Paper 025009. doi:10.1088/0964-1726/18/2/025009
- [18] Den Hartog, J. P., *Mechanical Vibrations*, McGraw–Hill, New York, 1956, p. 153.
- [19] Crandall, S., Karnopp, D., Kurtz, E. F., Jr., and Pridmore-Brown, D., *Dynamics of Mechanical and Electromechanical Systems*, McGraw–Hill, New York, 1968, p. 275.
- [20] Erturk, A., Anton, S. R., and Inman, D. J., "Piezoelectric Energy Harvesting from Multifunctional Wing Spars for UAVS, Part 1: Coupled Modeling and Preliminary Analysis," *Proceedings of SPIE*, San Diego, CA, Vol. 7288, 2009, Paper 72880C. doi:10.1117/12.815775
- [21] Stanton, S. C., McGehee, C. C., and Mann, B. P., "Nonlinear Dynamics for Broadband Energy Harvesting: Investigation of a Bistable Piezoelectric Inertial Generator," *Physica D: Nonlinear Phenomena*, Vol. 239, No. 10, 2010, pp. 640–653. doi:10.1016/j.physd.2010.01.019
- [22] Stanton, S. C., Erturk, A., Mann, B. P., and Inman, D. J., "Resonant Manifestation of Intrinsic Non-Linearity Within Electroelastic Micropower Generators," *Applied Physics Letters*, Vol. 97, No. 25, 2010, Paper 254101. doi:10.1063/1.3530449